

1 **Semi-quantitative determination of the Fe/Mg ratio in synthetic cordierite using**
2 **Raman spectroscopy**

3 REVISION 1

4 Authors: Udo Haefeker¹, Reinhard Kaindl², Peter Tropper¹

5

6 ¹Institute of Mineralogy and Petrography, University Innsbruck, Innrain 52, A-6020
7 Innsbruck, Austria.

8 E-mail: udo.haefeker@uibk.ac.at

9 ²Present address: MATERIALS – Institute for Surface Technologies and Photonics,
10 Functional Surfaces, JOANNEUM RESEARCH Forschungsgesellschaft mbH,
11 Leobner Straße 94, A-8712 Niklasdorf, Austria.

12

13 **ABSTRACT**

14 Investigations of H₂O-bearing synthetic well-ordered Mg-Fe-cordierites ($X_{\text{Fe}} = 0-1$)
15 with micro-Raman spectroscopy revealed a linear correlation between the Fe/Mg
16 ratio and the position of certain Raman peaks. In the range between 100 and 1250
17 cm^{-1} all peaks except for three peaks shift towards lower wavenumbers with
18 increasing X_{Fe} as a consequence of the substitution of the lighter Mg by the heavier
19 Fe atom on the octahedral sites and the associated structural changes. Selected
20 medium and strong peaks show a shift of 5 to 13 cm^{-1} , respectively. Based on recent
21 quantum-mechanical calculations (Kaindl et al. 2011) these shifts can be attributed to
22 specific vibrational modes in the cordierite structure, thus showing that the Mg-Fe
23 exchange affects the vibrational modes of tetrahedral, octahedral and mixed sites.
24 The peaks (wavenumber Mg-/ Fe-cordierite) at 122/111 cm^{-1} , 262/257 cm^{-1} , 430/418
25 cm^{-1} , 579/571 cm^{-1} , 974/967 cm^{-1} and 1012/1007 cm^{-1} were selected for detailed
26 deconvolution analysis. The shifts of these peaks were then plotted versus X_{Fe} and

27 regression of the data lead to the formulation of a set of linear equations. Assuming
28 ideal Fe-Mg mixing of the end-members and using linear peak shifts then allows the
29 development of calibration diagrams for the semi-quantitative determination of the
30 Fe-Mg contents of cordierite samples with Raman spectroscopy. In addition the effect
31 of different H₂O contents and the degree of Al-Si ordering on the Fe/Mg
32 determination were also investigated. Testing the calibration against data from six
33 well-characterized natural cordierite samples yielded excellent agreement.

34 **Keywords**

35 Raman spectroscopy, cordierite, Mg-Fe exchange, peak shift, Al-Si ordering.

36

37

INTRODUCTION

38 The Mg-Fe silicate cordierite with the idealized formula (Mg,Fe)₂Al₄Si₅O₁₈ x nH₂O
39 occurs as hexagonal, high-temperature and orthorhombic, low-temperature
40 polymorphs with disordered/ordered Al-Si distribution on the tetrahedral sites.
41 Cordierite is an important petrogenetic mineral because when in equilibrium with
42 other Mg-Fe-silicates the Mg/Fe ratio of cordierite can be used as a
43 geothermobarometer (e.g., Lonker 1981; Bhattacharya 1986; Kalt et al. 1999; Kalt
44 2000). Various amounts of volatiles like H₂O and CO₂ can also be incorporated into
45 the structural channels of cordierite, which allows paleofluid reconstructions (Harley
46 et al. 2002, Bul'bak and Shvedenkov 2005; Rigby et al. 2008). Most of the natural
47 cordierites are fully ordered and have the space group symmetry Cccm. Structurally,
48 six-membered rings of (Si,Al)O₄ are stacked along the crystallographic c-axis and
49 form channels, laterally and vertically linked by additional (Al, Si) tetrahedrons. The
50 octahedral coordinated M-sites, two different tetrahedral coordinated T-sites (T₁, T₂)
51 and the channel sites (Ch0, Ch1/4) are distinguished in the structure, according to
52 the general formula: (M)₂(T₁)₂(T₂)₂(T₃)₂(T₄)₂(T₅)₂(T₆)₂O₁₈(Ch0,Ch1/4),

53 where Si occupies the T₂₃, T₂₁ and T₁₆ sites and Al the remaining two T₁₁ and T₂₆
54 sites. Structural refinement and Al/Si-ordering was investigated by various authors
55 (e.g., Gibbs 1966; Langer und Schreyer 1969; Meagher and Gibbs 1977; Cohen et
56 al. 1977; Hochella et al. 1979; Putnis 1980; Wallace and Wenk 1980; Putnis 1983;
57 Armbruster 1985; Malcherek et al. 2001; Bertoldi et al. 2004 and references therein;
58 Miletich et al. 2010). The Mg and Fe²⁺ ions are located in the octahedral coordinated
59 M-sites and their mixing is assumed to be ideal (e.g., Boberski and Schreyer 1990);
60 90 to 99% Fe²⁺ occupies the octahedral site (Khomenko et al. 2001). The amount of
61 Fe³⁺ in natural cordierites is insignificantly low (Geiger et al. 2000). The incorporation
62 of Fe²⁺ in exchange for Mg leads to multiple structural changes: 1) expansion of the
63 mean M-O-distances within the octahedra leads to the elongation of the unit cell in a-
64 and b-directions and 2) T₁₁-O distances decrease slightly, leading to a contraction
65 along the c-axis (e.g., Wallace and Wenk 1980; Armbruster 1985; Boberski and
66 Schreyer 1990; Malcherek et al. 2001; Geiger and Grams 2003). Raman and FT-IR
67 spectroscopic methods were already used by several authors to investigate and
68 describe different properties of cordierite, like polymorphism (Langer and Schreyer
69 1969), volatile content (Vry et al. 1990; Kalt 2000; Kolesov and Geiger 2000;
70 Yakubovich et al. 2004; Bul'bak and Shvedenkov 2005; Khomenko and Langer 2005;
71 Kaindl et al. 2006; Kolesov 2006; Nasdala et al. 2006; Rigby et al. 2008; Weikusat et
72 al. 2010), Al-Si ordering (McMillan et al. 1984; Güttler et al. 1989; Poon et al. 1990),
73 structural heterogeneity and energetic and structural changes under high pressure
74 (Geiger and Grams 2003; Likhacheva et al. 2011). Local structural heterogeneities in
75 natural Fe-Mg-cordierites and their thermodynamic mixing properties have also been
76 investigated with IR spectroscopy (Geiger and Grams 2003). Quantum-mechanical
77 calculations of the Raman spectra of Mg- and Fe-cordierites have also been done for
78 a detailed peak assignment and a theoretical description of the effects of the Mg-Fe

79 exchange and Al-Si ordering (Kaindl et al. 2011). Semi-quantitative techniques for
80 the determination of chemical compositions, based on the shifts of vibrational modes
81 within certain mineral solid solutions, have been presented for example for garnets,
82 olivines and pyroxenes (Geiger and Grams 2003; Smith 2005; Kuebler et al. 2006;
83 Bersani et al. 2009; Stalder et al. 2009). The aim of this work is the detailed Raman
84 spectroscopic description of structural changes in H₂O-bearing synthetic cordierite as
85 a consequence of Mg-Fe-exchange and the development of semi-quantitative
86 calibrations for the determination of the Mg/Fe ratio in natural and synthetic cordierite
87 samples.

88

89

EXPERIMENTAL METHODS

90 **Synthesis of Mg-Fe-cordierites and sample preparation**

91 Cordierites with the composition (Mg,Fe)₂Al₄Si₅O₁₈ x nH₂O were synthesized using
92 annealing and hydrothermal techniques. SiO₂ nanopowder (99.5%, metals basis,
93 Aldrich), Al₂O₃ (gamma, 99,997%, metals basis, Alfa Aesar), MgO (Art. 5865, Merck),
94 FeO (Iron (II) oxide, 99.5%, metals basis, Alfa Aesar), Fe (Art. 3819, Merck) and
95 graphite powder were used for the synthesis. The synthesis of the hydrous Fe- and
96 the dry Mg-end-member has been described in detail by Kaindl et al. (2011). To
97 obtain H₂O-bearing samples, orthorhombic Mg-cordierite was treated hydrothermally
98 in a welded gold capsule together with H₂O at 700 °C and 0.2 GPa for 7 days. The
99 full synthesis sequence was: stoichiometric glass → nucleation/formation of “beta-
100 cordierite” → disordered hexagonal anhydrous cordierite → ordered orthorhombic
101 anhydrous cordierite → ordered orthorhombic hydrous cordierite. The transition from
102 hexagonal to orthorhombic Mg-cordierite caused the formation of a patchy “tweed”
103 microstructure in the cordierite crystals (Putnis 1983; Armbruster 1985; Putnis et al.
104 1987; Blackburn and Salje 1999).

105 Powdered glass with Mg-cordierite stoichiometry and the oxides FeO, Al₂O₃ and SiO₂
106 in various fractions were used as starting material for the synthesis of hydrous
107 cordierite crystals with X_{Fe} [= Fe/(Fe + Mg)] ranging from 0.1 to 0.4. Sealed buffered
108 double capsules were then used, with IW (iron/wüstite)-buffer and H₂O in the outer
109 gold-capsule and the starting material and H₂O in an inner Ag₇₀Pd₃₀ capsule. The
110 experimental conditions were 700 °C and 0.2 GPa and the experimental duration was
111 7 days. For the synthesis of hydrous crystals with $X_{\text{Fe}} = 0.5-0.8$ cordierite glasses
112 with $X_{\text{Fe}} = 0.5-0.8$ were produced. The glasses were then tempered in a welded gold
113 capsule together with graphite powder for 16 to 24 hours at 900 °C to obtain the
114 unordered hexagonal cordierite. This cordierite was then loaded together with H₂O in
115 a hydrothermal apparatus at 700 °C and 0.25-0.3 GPa for 7 days to obtain well-
116 ordered H₂O-bearing orthorhombic cordierite. The synthesis were done in buffered
117 capsules with IW-buffer and H₂O in the outer gold capsules and the starting material
118 and H₂O in the inner Ag₇₀Pd₃₀ capsules.

119

120 **Electron microprobe analysis**

121 For electron microprobe analysis all synthesis products were embedded in an epoxy
122 mount, grinded and finally polished using a 1 µm diamond suspension. The
123 orientation of the crystals from run products was random. The JEOL JXA 8100
124 SUPERPROBE at the Institute of Mineralogy and Petrography at the University of
125 Innsbruck was used for the chemical analyses of the glasses, the intermediate run
126 products and the final cordierite samples. Analytical conditions for the wavelength
127 dispersive measurements were 15 kV acceleration voltage and a beam current of 10
128 nA. Counting times for all elements were 20 seconds for the peak and 10 seconds for
129 the background. For the calibration synthetic (corundum) and natural (almandine,
130 quartz, orthoclase and diopside) microprobe standards were used. Mineral formulae

131 were calculated on the anhydrous basis of 18 oxygens. Some measurements were
132 performed in point mode due to the small grain size and inhomogeneities in the
133 synthesis materials. Depending on the elements and their concentrations the
134 standard deviation of the measurements of each element is between 0.34 and
135 1.79%. For precise correlation we used BSE imaging to be able to correlate the
136 locations of the analyzed spots with the locations of the subsequent Raman
137 spectroscopic investigations.

138

139 **X-ray powder diffraction**

140 Powder X-ray diffraction for the determination of the lattice parameters and the
141 degree of Al-Si ordering in the Mg-cordierite samples was done with a Stoe STADI-
142 MP diffractometer system in bisecting transmission geometry in a 2Θ range from 2 to
143 129.8° in steps of 0.009° . The system is equipped with a "Mythen" 1k detector and an
144 asymmetric Ge(111)-monochromator yielding a strictly monochromatic CuK α 1
145 radiation. For the Fe-end-member a Bruker D8 Discover system with Bragg-
146 Brentano-geometry over a 2Θ range from 5° to 80.25° in steps of 0.009° was used.
147 The system is equipped with a copper target and a silicon-strip-detector. Rietveld
148 calculations and LeBail fits were done using the program FullProf. 2k (Rodriguez-
149 Carvajal, 2011). The background was determined by linear interpolation between a
150 set of breakpoints with refineable heights. Intensities within 10 times the full-width at
151 half-maximum of a peak were considered to contribute to the central reflection.
152 Thompson–Cox–Hastings pseudo-Voigt functions were chosen for the simulation of
153 the peak shape, including an asymmetry correction following Finger et al. (1994).
154 For the hydrous orthorhombic Mg-end-member the cell parameters $a = 17.055$, $b =$
155 9.724 , $c = 9.348$ and a distortion index (Miyashiro, 1957) of ≈ 0.24 were obtained. The

156 cell dimensions of the hydrous orthorhombic Fe-end-member are $a = 17.244$, $b =$
157 9.828 , $c = 9.288$ and the distortion index is ≈ 0.24 .

158

159 **Raman Spectroscopy**

160 Due to small grain sizes and the patchy microstructure of synthetic cordierite all
161 measurements were done on randomly oriented crystals. Unpolarized and polarized
162 spectra of synthetic cordierite crystals were measured on a Labram HR-800 confocal
163 Raman-spectrometer by HORIBA, using the 532 nm excitation wavelength of a 30
164 mW Nd:YAG laser through a 100 \times objective with a numerical aperture of 0.9. The
165 size and power of the laser spot on the surface was approximately 1 μm and 5 mW,
166 respectively. The confocal pinhole aperture was 1000 μm and the width of the
167 entrance slit 100 μm . A grating with 1800 lines/mm was used to disperse the
168 scattered Raman light, which was detected by an open-electrode charge-coupled
169 device with 1024 \times 256 pixels, each with a size of 43 μm . The spectral resolution of
170 1.4 cm^{-1} was determined by measuring the Rayleigh line. Accuracy of the Raman line
171 shifts was checked by regular measurements of the emission lines of a Ne spectral
172 calibration lamp and the deviation was $\pm 0.24 \text{ cm}^{-1}$. Background and Raman peaks
173 were fitted using the built-in spectrometer software LabSpec with the line-segments
174 baseline correction and convoluted Gauss-Lorentz functions. The spectra were
175 recorded for 2 x 200 seconds in the area of 100 – 1250 cm^{-1} using unpolarized (no
176 additional polarizers used) and polarized laser light (polarizers were used for
177 excitation and the scattered Raman light). Deconvolution is not trivial since the
178 spectra of cordierite are characterized by a) complex peak overlaps forming band
179 systems (envelopes) and by b) peak broadening in Fe-rich samples. In the
180 unpolarized spectra most of the band systems are dominated by intense peaks and
181 cordierite shows a strong spectroscopic anisotropy. While peak intensities strongly

182 depend on the orientation of the crystal to the polarisation plane of the laser light,
183 there are no orientation effects of the peak positions though. The contribution of
184 individual peaks to the band system varies with the overall orientation of the crystal
185 thus influencing band shapes and positions. For the determination of individual peaks
186 and their positions within the band systems each sample was measured twice using
187 polarized laser light for excitation and a polarizer for the scattered light set
188 perpendicular and parallel to the laser polarization. This filtering-procedure was
189 necessary for a successful deconvolution process because removing specific peaks
190 within complex band systems facilitates the identification of others. In addition, the
191 area between 100 and 350 cm^{-1} , which shows a higher peak density, was measured
192 for 2 x 200 sec in a high-resolution mode with an entrance slit set to 20 μm . The sub-
193 pixel acquisition function was then used to increase the peak definition by providing
194 five-times more data points. The information gained from the detailed measurements
195 was used together with the calculated peak positions by Kaindl et al. (2011) thus
196 providing the initial values for the deconvolution of the band systems. Multi-peak
197 fitting with simultaneous and stepwise fitting of several narrow peaks was necessary
198 for the more complex band systems (Bradley, 2007; Knorr, 2011). The errors of the
199 deconvolution process were determined empirically by repeating the curve-fit routine
200 for all six peaks of Fe-cordierite used in the calibration diagrams in an unpolarized
201 spectrum for 10 times. The Fe-end-member was selected because the effect of peak-
202 broadening and peak-overlapping is higher compared to Mg-bearing cordierites. For
203 the calibration the peak position of the unpolarized and polarized measurements
204 were used. Detailed chemical analyses and descriptions of the investigated natural
205 cordierite samples can be found in Bertoldi et al. (2004).

206

207

RESULTS

208 **Mg-cordierite**

209 The Raman spectra of 16 randomly oriented cordierite samples with compositions
210 from $X_{\text{Fe}} = 0$ to 1 were investigated between 100 and 1250 cm^{-1} . Characteristic for
211 the Raman spectra of Mg-Fe-cordierites are regions with dominant peaks and band
212 systems containing various numbers of overlapping peaks, which show a diagnostic
213 shift towards lower wavenumbers with increasing Fe-contents. Exceptions are the
214 low-intensity bands around 330, 909 and 960 cm^{-1} . After a close investigation of the
215 Raman spectra of all available samples in different orientations we selected six
216 peaks, which seem to be most suitable for the development of a calibration curve
217 because of their accessibility in terms of intensities, orientation effects and peak shift
218 values (Fig. 1). In Mg-cordierite these are medium- to high-intensity peaks at 121 cm^{-1}
219 (A), 261.5 cm^{-1} (B), 430 cm^{-1} (C), 579 cm^{-1} (D), 974 cm^{-1} (E) and 1012.5 cm^{-1} (F).
220 The peak at 121 cm^{-1} is the dominant peak in the complex band system in the region
221 from 100 to 135 cm^{-1} . Towards lower wavenumbers we find medium- to low-intensity
222 peaks at 118 and 116 cm^{-1} . Adjacent to a small gap between 114 and 109 cm^{-1} a
223 low-intensity peak follows at 107 cm^{-1} . Towards higher wavenumbers the peak at 121
224 cm^{-1} is strongly overlapped by a second intense peak at 123 cm^{-1} , followed by
225 medium- to high-intensity peaks at 126 cm^{-1} , 129 cm^{-1} and 131 cm^{-1} .
226 The peak at 261.5 cm^{-1} is the most intense peak in the band system in the region 230
227 to 275 cm^{-1} containing 8 individual peaks. Towards lower wavenumbers this peak is
228 overlapped by a high-intensity peak at 260 cm^{-1} followed by a low-intensity peak at
229 256 cm^{-1} . A group of three medium- to low-intensity peaks follows at 243 cm^{-1} , 242
230 cm^{-1} and 241 cm^{-1} . Towards higher wavenumbers this peak is overlapped by
231 medium- to low-intensity peaks at 265 cm^{-1} and 269 cm^{-1} .
232 The medium-intensity peak at 430 cm^{-1} is flanked by a low-intensity peak at 436 cm^{-1} .

233 The high-intensity peak at 579 cm^{-1} is part of a band system with 5 individual peaks.
234 Towards lower wavenumbers it is overlapped by the medium-intensity peak at 566
235 cm^{-1} and a high-intensity peak at 557 cm^{-1} , followed by a low-intensity peak at 546
236 cm^{-1} . Towards higher wavenumbers this peak is overlapped by a low-intensity peak
237 at 592 cm^{-1} . The high-intensity peak at 974 cm^{-1} has a neighbouring peak at 952 cm^{-1}
238 with medium intensity. The medium- to high-intensity peak follows at 1012.5 cm^{-1} .
239 The experimental data are in good agreement with the calculated cordierite Raman
240 spectra by Kaindl et al. (2011), which allow the unambiguous assignment of the
241 peaks A – E. According to Kaindl et al. (2011) peak A results from the modes
242 deforming and rotating mainly the T_{16} site. Peak B results from the bending modes of
243 both the Si- and Al- tetrahedral and the M-octahedral sites. Peak C is a result from
244 the bending of the T_{26} site. The split bands between 500 and 630 cm^{-1} including
245 band (D) are related to the bending vibrations of the T_{26} , T_{21} and T_{23} and the
246 stretching of the M- and T_{26} -sites. Peak E is caused by the stretching of the T_{21} and
247 T_{16} sites. Peak F is caused by the stretching of the T_{21} and T_{23} ring-tetrahedra as
248 well as the T_{16} tetrahedron, which connects two M-sites. A complete band
249 assignment for both cordierite Fe- and Mg-end-members can be found in Kaindl et al.
250 (2011).

251

252 **Fe-cordierite and peak shifts**

253 In the spectra of the Fe-end-member the equivalent peaks can be found at 110.5 cm^{-1}
254 (A') , 256.5 cm^{-1} (B') , 418 cm^{-1} (C') , 571.5 cm^{-1} (D') , 967 cm^{-1} (E') and 1007.5 cm^{-1}
255 (F') . Figure 2A-F shows the peak shifts as a function of the Fe-content for the 16
256 samples listed in Table 1. Peaks A/A' and C/C' show the highest shifts with 11 and
257 12 cm^{-1} , while peaks B/B' and E/E' show the lowest shifts with 5 cm^{-1} .

258 Regressions of the data of peaks A – F lead to the following linear equations:

259

$$260 \quad (A) X_{Fe} = \frac{P_{(A)} - 121.67}{-10.814} \quad (B) X_{Fe} = \frac{P_{(B)} - 261.52}{-5.2198}$$

$$261 \quad (C) X_{Fe} = \frac{P_{(C)} - 430.48}{-12.526} \quad (D) X_{Fe} = \frac{P_{(D)} - 579.02}{-6.5019}$$

$$262 \quad (E) X_{Fe} = \frac{P_{(E)} - 973.8}{-6.7901} \quad (F) X_{Fe} = \frac{P_{(F)} - 1012.9}{-4.3776}$$

263

264 The standard deviations $2\sigma_1$ (hardware uncertainties) and $2\sigma_2$ (fitting procedures) for
265 the Raman positions were calculated with equation 1, the overall standard deviations
266 $2\sigma_{overall}$ were calculated with equation 2:

$$267 \quad 1.) \sigma_{1,2} = \sqrt{\frac{\sum (x - \bar{x})^2}{(n-1)}} \quad 2.) \sigma_{overall} = \sqrt{\sigma_1^2 + \sigma_2^2}$$

268 The 2σ standard deviations are given in figure 2A-F. The calculations based on a
269 spectrum of Fe-cordierite yielded a significantly higher error in the peak position and
270 thus in the prediction of X_{Fe} due to the uncertainties using spectral curve fitting
271 procedures compared to Mg-cordierite.

272

273

DISCUSSION

274 Peak shifts and structural changes in Mg-Fe-cordierite

275 The general trend of downshift of peaks in Fe-cordierite compared to their
276 equivalents in Mg-cordierite is probably caused by decreasing mean M-O and
277 increasing T_1 -O bond distances (Malcherek et al. 2001). However, for individual
278 peaks the interplay seems to be extremely complex: The equivalent peaks C/C' for
279 example result both from vibrations of Al in the T_2 6 site. Peak A in contrast in Mg-
280 cordierite is assigned to Si in the T_1 6-, T_2 1- and T_2 3-site whereas peak A' in Fe-
281 cordierite to Al in the T_1 1- and Fe in the M-site (Kaindl et al. 2011). This complexity is

282 reflected in the larger number of Gauss-Lorentz functions necessary to deconvolute
283 peaks A/A'. Furthermore, one has to take into account the limited accuracy of peak
284 assignments by quantum mechanical calculations (up to $\pm 16 \text{ cm}^{-1}$ for individual
285 peaks), substitutions of Mg and Fe^{2+} for Al and compositional dependence of Al-Si
286 ordering (Malcherek et al. 2001; Kaindl et al. 2011). Further discussions are therefore
287 restricted to the practical aspects of the observed dependencies between peak shifts
288 and Fe-contents.

289

290 **Influences on the Raman measurements I: the effects of Al-Si ordering and H₂O**
291 **contents**

292 Natural Mg-Fe-cordierites are mainly orthorhombic with a fully ordered Al/Si
293 distribution on the tetrahedral sites and distortion indices (Miyashiro 1957) between
294 0.21 and 0.27 (e.g., Hochella 1979; Armbruster and Bloss 1981). Since the
295 disordered hexagonal polymorph (distortion index 0) occurs as an intermediate phase
296 in the annealing experiments and was used as starting material for some of the
297 hydrothermal experiments it was necessary to reinvestigate the effect of Al/Si
298 ordering on the Raman peak positions, mainly because the distortion indices of our
299 synthetically grown hydrous cordierites do not exceed values of ≈ 0.245 . The
300 hexagonal to orthorhombic transition and related changes in the Raman spectra (Fig.
301 1) can be described with an increase of the number of Raman active modes from 10
302 to 33, peak-sharpening accompanied by intensity increase and the simultaneous
303 splitting of the strong band at 567 cm^{-1} into three bands at 557, 564 and 578 cm^{-1}
304 (McMillan et al. 1984; Poon et al. 1990). Kaindl et al. (2011) calculated five modes in
305 this energy region for the ordered orthorhombic polymorph. Al-Si ordering in synthetic
306 annealed cordierite is a function of temperature and time (Putnis and Bish 1983,
307 McMillan et al. 1984). While longer annealing times at temperatures of $1200 \text{ }^\circ\text{C}$

308 results in increasing distortion indices, the Raman spectra of cordierites do not
309 change significantly after the transition from hexagonal to orthorhombic symmetry.
310 The spectra of orthorhombic cordierite samples with annealing times of 3 h and 348 h
311 at 1400 °C show no significant differences of the peak positions in the area between
312 100 and 1250 cm^{-1} , only the split band at $\approx 557 \text{ cm}^{-1}$ shows a small shift of $<1 \text{ cm}^{-1}$
313 towards lower wavenumbers.
314 The hydrothermal experiments with glass or disordered cordierite as starting material
315 have shown that 1. the ordering process depends of the amount of H_2O present in
316 the capsule during the hydrothermal synthesis at relatively low temperatures of 700
317 °C . Experiments with no or very low amounts of H_2O available show no or only low
318 degrees of Al-Si ordering. 2. The size of the starting material also has an effect on
319 the ordering process. Figure 3A and 3B show Raman data at the rim of a
320 hydrothermally-treated stoichiometric Fe-cordierite glass fragment with a size of
321 several 100 μm . The split peak region between 500 and 650 cm^{-1} and the intensities
322 of the H_2O peak around 3600 cm^{-1} are shown across a distance of 80 μm from the
323 rim into the interior. The amount of H_2O incorporated and the peak-splitting distance
324 decrease with increasing distance to the fluid contact zone at the outer rim. The
325 profiles suggest a maximum penetration depth limit of water of about 20 μm .
326 Investigations of anhydrous and hydrous orthorhombic Mg-cordierite confirm that
327 H_2O incorporation does not affect the position of the Raman peaks except for one
328 peak at $\approx 1180 \text{ cm}^{-1}$, which shifts towards lower wavenumbers with increasing H_2O
329 contents. Therefore, this peak was excluded for Mg-Fe determination since the
330 amount of H_2O in the channels of natural cordierites is variable (e.g., Bertoldi et al.,
331 2004).

332

333 **Influences on the Raman measurements II: the nature of the starting materials**

334 Some of the electron microprobe analyses of Fe-rich samples gave low totals of
335 95.68 - 97.50 wt.%. All of the synthetic cordierites used in this study contain water
336 but the amount of channel H₂O is insufficient to explain these deviations. A possible
337 reason could be the presence of Fe³⁺ within the structure, which was not considered
338 in mineral formula calculations. Attempts for Fe³⁺ determinations with Mössbauer-
339 spectroscopy failed due to too little amounts of sample material.

340 Electron microprobe analyses showed that the synthesis products of our Mg-Fe-
341 experiments are in some cases inhomogeneous with variations of $\pm X_{\text{Fe}} \leq 0.08$ within
342 the same capsule. We assume that the short synthesis times prevented pervasive
343 equilibration within the capsules. To avoid further uncertainties related to
344 inhomogeneous compositions in the intermediate Fe-Mg range structural data with
345 powder X-ray methods were only collected for the homogeneous Fe- and Mg-end-
346 members.

347 High-resolution Raman investigations of the region 100-135 cm⁻¹ of Mg-cordierite
348 reveal a higher peak density than expected since quantum-mechanical calculations
349 by Kaindl et al. (2011) predicted six peaks, but the experimental data show at least
350 eight individual peaks in this area. This might result from an imperfect cordierite
351 structure with defects and/or distortions, activating otherwise forbidden bands due to
352 breaking of selection rules. Such theoretically not allowed bands were observed for
353 example in halides, borosilicate feldspar, zeolites, silica glasses, dodecaborides and
354 GeO₂ (Benedek and Nardelli 1967; Bäuerle 1973; Best et al. 1994; Mihailova et al.
355 2005; Nesterova et al. 2005; Werheit et al. 2011; Kaindl et al. 2012).

356

357 **Application of the calibration to natural samples**

358 All of the presented correlation diagrams (Fig. 2A-F) can be used for semi-
359 quantitative determinations of X_{Fe} in natural samples. The main difficulty when

360 working with Raman spectra of cordierites are peak-overlaps and hence the precise
361 determination of individual peak positions. For practical purposes and in order to
362 reduce the errors introduced by the fitting procedures we recommend the use of
363 calibration diagrams 2C, D, E and F, although the correlation coefficients of all six
364 regression equations are close to 1. Band deconvolution of these peaks is less
365 complex and time consuming, the other diagrams (2A, B) can be used when the
366 results are inconsistent or higher precision is necessary. The complexity of the two
367 band systems in the region $100 - 350 \text{ cm}^{-1}$ is a potential source of error during the de-
368 convolution process.

369 Figure 4 shows a calibration diagram based upon peak D at 575 cm^{-1} . The obtained
370 peak positions of six natural well-characterized cordierite samples were added to the
371 diagram and are in good agreement with the experimental data. The Fe-Mg
372 composition of the samples TA-1 with $X_{\text{Fe}} = 0.04$, WYO-2 with $X_{\text{Fe}} = 0.10$, C005 with
373 $X_{\text{Fe}} = 0.19$, VS3 with $X_{\text{Fe}} = 0.24$, HO6 with $X_{\text{Fe}} = 0.54$ and TUB-1 with $X_{\text{Fe}} = 0.76$
374 could be adequately reproduced by the developed Raman technique. The good
375 reproducibility of these natural samples also shows that chemical deviations from the
376 ideal stoichiometric composition have no effect on the measurements so far. The
377 natural samples contain minor amounts of Mn, Be, Li and Zn as well as channel
378 cations and volatiles (Na, K, CO_2).

379

380

CONCLUSIONS

381 This study confirmed that Mg-Fe exchange in cordierite causes linear and non-linear
382 structural changes, which are manifested as shifts of Raman peaks. The six Raman
383 peaks investigated in this study shift linearly with Mg-Fe exchange and were fitted to
384 obtain calibration equations (equations A-F). The presented calibrations are based
385 on a set of synthetic hydrous Mg-Fe-cordierites and allow fast and non-destructive

386 semi-quantitative X_{Fe} determinations of cordierite in thin sections, single crystals and
387 hand specimen without additional sample preparation. Applicability of the method
388 was checked on natural cordierite with minor amounts of Be, Li or Mn and various
389 amounts of channel cations (Na, K) and volatiles (CO_2 , N_2). The good agreement of
390 X_{Fe} derived by independent methods and Raman spectroscopy confirms that
391 incorporation of these components influences the cordierite structure to a much
392 lesser extent than Fe-Mg exchange and Si-Al order-disorder.

393

394

ACKNOWLEDGEMENTS

395 We thank Martina Tribus for her help with the electron microprobe analysis, Jürgen
396 Konzett for the valuable advice concerning the experiments and Daniel Többens for
397 his help with X-ray powder analysis. This study was funded by the Austrian Science
398 Fund (FWF): [P22013-N21].

399

400

401

402

403

404

405

406

407

408

409

410

411

412

REFERENCES

413

414 Armbruster, T. (1985) Crystal structure refinement, Si, Al-ordering, and twinning in

415 "Pseudo-hexagonal" Mg-cordierite. *Neues Jahrbuch fuer Mineralogie.*

416 *Monatshefte*, 255-267.

417 Armbruster, T. and Bloss, F.D. (1981) Mg-Cordierite: Si/Al ordering, optical

418 properties, and distortion. *Contributions to Mineralogy and Petrology*, 77, 332-

419 336.

420 Armbruster, T. and Bloss, F.D. (1982) Orientation and effects of channels H₂O and

421 CO₂ in cordierite. *American Mineralogist*, 67, 284-291.

422 Benedek, G., and Nardelli, G.F. (1967) Raman scattering by color centers. *Physical*

423 *Review*, 154(3), 872-876.

424 Bersani, D., Andò, S., Vignola, P., Molfiori, G., Marino, I.-G., Lottici, P. P., Diella, V.

425 (2009) Micro-Raman spectroscopy as a routine tool for garnet analysis.

426 *Spectrochimica Acta Part A*, 73, 484-491.

427 Bertoldi, C., Proyer, A., Garbe-Schönberg, D., Behrens, H., and Dachs, E. (2004)

428 Comprehensive chemical analyses of natural cordierites: implications for

429 exchange mechanisms. *Lithos*, 78, 389-409.

430 Best, S.P., Clark, R.J.H., Hayward, C.L., and Withnall, R. (1994) Polarized single-

431 crystal Raman spectroscopy of danburite, CaB₂Si₂O₈. *Journal of Raman*

432 *Spectroscopy*, 25(7-8), 557-563.

433 Bhattacharya, A. (1986) Some geobarometers involving cordierite in the FeO-Al₂O₃-

434 SiO₂ (±H₂O) system: refinements, thermodynamic calibration, and

435 applicability in granulite-facies rocks. *Contributions to Mineralogy and*

436 *Petrology*, 94, 387-394.

- 437 Blackburn, J. F. and Salje, K. H. (1999) Sandwich domain walls in cordierite: a
438 computer simulation study. *Journal of Physics: Condensed Matter*, 11, 4747-
439 4766.
- 440 Boberski, C. and Schreyer, W. (1990) Synthesis and water contents of Fe²⁺-bearing
441 cordierites. *European Journal of Mineralogy*, 2, 565-584.
- 442 Bradley, M. (2007) *Curve Fitting in Raman and IR Spectroscopy: Basic Theory of*
443 *Line Shapes and Applications*. Thermo Fisher Scientific, Madison, USA,
444 Application Note: 50733.
- 445 Bäuerle, D. (1973) Vibrational spectra of electron and hydrogen centers in ionic
446 crystals. *Springer Tracts in Modern Physics*, 68, 76-160.
- 447 Cohen, J.P., Ross, F.K., and Gibbs, G.V. (1977) An X-ray and neutron diffraction
448 study of hydrous low cordierite. *American Mineralogist*, 62, 67-78.
- 449 Finger, L. W., Cox, D. E. and Jephcoat, A. P. (1994) A Correction for Powder
450 Diffraction Peak Asymmetry Due to Axial Divergence. *Journal of Applied*
451 *Crystallography*, 27, 892-900.
- 452 Geiger, C.A. (2001) Cordierite IV: structural heterogeneity and energetics of Mg-Fe
453 solid solutions. *Contributions to Mineralogy and Petrology*, 145, 752-764.
- 454 Geiger, C.A. and Grams, M. (2003) Cordierite IV: structural heterogeneity and
455 energetics of Mg-Fe solid solutions. *Contributions to Mineralogy and*
456 *Petrology*, 145, 752-764.
- 457 Geiger, C.A., Rager, H., Czank, M. (2000) Cordierite III: the site occupation and
458 concentration of Fe³⁺. *Contributions to Mineralogy and Petrology*, 140, 344-
459 352.
- 460 Gibbs, G.V. (1966) The polymorphism in cordierite I: the crystal structure of low
461 cordierite. *American Mineralogist*, 51, 1068-1087.

- 462 Güttler, B., Salje, E. and Putnis, A. (1989) Structural States of Mg Cordierite III:
463 Infrared Spectroscopy and the Nature of the Hexagonal-Modulated Transition.
464 Physics and Chemistry of Minerals, 16, 365-373.
- 465 Harley, S.L., Thompson, P., Hensen, B.J., and Buick, I.S. (2002) Cordierite as a
466 sensor of fluid conditions in high-grade metamorphism and crustal anatexis.
467 Journal of Metamorphic Geology, 20, 71-86.
- 468 Hochella, M.F., Brown, G.E., Ross, F.K. and Gibbs, G.V. (1979) High-temperature
469 crystal chemistry of hydrous Mg- and Fe-cordierites. American Mineralogist,
470 64, 337-351.
- 471 Kaindl, R., Tropper, P., and Deibl, I. (2006) A semi-quantitative technique for
472 determination of CO₂ in cordierite by Raman spectroscopy in thin sections.
473 European Journal of Mineralogy, 18, 331-335.
- 474 Kaindl, R., Többsens D. and Haefeker U. (2011) Quantum-mechanical calculations of
475 the Raman spectra of Mg- and Fe-cordierite. American Mineralogist, 96, 1568-
476 1574.
- 477 Kaindl, R., Többsens, D., Penner, S., Bielz, T., Soisuwan, S., and Klötzer, B. (2012)
478 Quantum mechanical calculations of the vibrational spectra of the quartz- and
479 rutile-type GeO₂. Physics and Chemistry of Minerals, 39, 47-55.
- 480 Kalt, A., Berger, A. and Blümel, P. (1999) Metamorphic evolution of cordierite-bearing
481 migmatites from the Bayerische Wald (Variscan Belt, Germany). Journal of
482 Petrology, 40, 601-627.
- 483 Kalt, A. (2000) Cordierite channel volatiles as evidence for dehydration melting: an
484 example from high-temperature metapelites of the Bayerische Wald (Variscan
485 belt, Germany). European Journal of Mineralogy, 12, 987-998.
- 486 Khomenko, V.M., Langer, K. And Geiger, C. (2001) Structural locations of the iron
487 ions in cordierite. Contributions to Mineralogy and Petrology, 141, 381-396.

- 488 Khomenko, V.M. and Langer, K. (2005) Carbon oxides in cordierite channels:
489 Determination of CO₂ isotopic species and CO by single crystal IR
490 spectroscopy. American Mineralogist, 90, 1913-1917.
- 491 Knorr, B.M. (2011) Examples in Peak Fitting. Seminar in Modern Physics.
492 Department of Physics, Lehigh University, Bethlehem, PA 18015.
- 493 Kolesov, B.A. (2006) Raman spectra of single H₂O molecules isolated in cavities of
494 crystals. Journal of Structural Chemistry, 47, 21-34.
- 495 Kolesov, B.A. and Geiger, C.A. (2000) Cordierite II: The role of CO₂ and H₂O.
496 American Mineralogist, 85, 1265-1274.
- 497 Kuebler, K. E., Jolliff, B. L., Wang, A., Haskin, L. A. (2006) Extracting olivine (Fo-Fa)
498 compositions from Raman spectral peak positions. Geochimica et
499 Cosmochimica Acta, 70, 6201-6222.
- 500 Langer, K. and Schreyer, W. (1969) Infrared and powder X-ray diffraction studies on
501 the polymorphism of cordierite, Mg₂(Al₄Si₅O₁₈). American Mineralogist, 54,
502 1442-1459.
- 503 Likhacheva, A. Y., Goryainov, S. V., Krylov, A. S., Bul'bak, T. A. and Prasad, S. R.
504 (2011) Raman spectroscopy of natural cordierite at high water pressure up to
505 5 GPa. Journal of Raman Spectroscopy, published online in Wiley Online
506 Library.
- 507 Lonker, S. W. (1981) The P-T-X relations of the cordierite-garnet-sillimanite-quartz
508 equilibrium. American Journal of Science, 63, 1056-1090.
- 509 Malcherek, T., Domeneghetti, M. C., Tazzoli, V., Ottolini, L., McCammon, C. And
510 Carpenter, M. A. (2001) Structural properties of ferromagnesian cordierites.
511 American Mineralogist, 86, 66-79.

- 512 McMillan, P., Putnis, A., and Carpenter, M.A. (1984) A Raman-Spectroscopic Study
513 of Al-Si Ordering in Synthetic Magnesium Cordierite. *Physics and Chemistry of*
514 *Minerals*, 10, 256-260.
- 515 Meagher, E.P. and Gibbs, G.V. (1966) The polymorphism of cordierite II: The crystal
516 structure of indialithe. *Canadian Mineralogist* , 15, 43-49.
- 517 Mihailova, B., Valtchev, V., Mintova, S., Faust, A.C., Petkov, N., and Bein, T. (2005)
518 Interlayer stacking disorder in zeolite beta family: a Raman spectroscopic
519 study. *Physical Chemistry Chemical Physics*, 7(14), 2756-2763.
- 520 Miletich, R., Gatta, G.D., Redhammer, G.J., Burchard, M., Meyer, H.P., Weikusat, C.,
521 Rotiroti, N., Glasmacher, U.A., Trautmann, C., Neumann, R. (2010) Structure
522 alterations in microporous (Mg,Fe)₂Al₄Si₅O₁₈ crystals induced by energetic
523 heavy-ion irradiation. *Journal of Solid State Chemistry*, 183, 2372-2381.
- 524 Miyashiro, A. (1957) Cordierite-indialite relations. *American Journal of Sciences*, 255,
525 43-62.
- 526 Mirwald, P., Kirchner, A. (1984) Zum Ordnungs-/Unordnungsverhalten von Mg-
527 Cordierit zwischen 1400 °C und dem Schmelzpunkt (1463 °C). *Fortschritte in*
528 *der Mineralogie*, 62 (Beiheft 1), 157-9.
- 529 Nasdala, L., Wildner, M., Wirth, R., Groschopf, N., Pal, D.C., Möller, A. (2006) Alpha
530 particle haloes in chlorite and cordierite. *Mineralogy and Petrology*, 86, 1-27.
- 531 Nesterova, Z.V., Melo Melchor, G., and Alexandrov, I.V. (2005) Medium-range
532 ordering in glass structures as a background of photosensitivity in silica fibers.
533 *Journal of Non-Crystalline Solids*, 351(52–54), 3789-3796.
- 534 Poon, W.C.K., Putnis, A., and Salje, E. (1990) Structural states of Mg cordierite: IV.
535 Raman spectroscopy and local order parameter behaviour. *Journal of Physics:*
536 *Condensed Matter*, 2, 6361-6372.

- 537 Putnis, A. (1980) Order-modulated structures and the thermodynamics of cordierite
538 reactions. *Nature*, 287, 128-131.
- 539 Putnis, A. (1983) The mechanism and kinetics of Al, Si ordering in Mg-cordierite.
540 *American Mineralogist*, 68, 60-65
- 541 Putnis, A., Salje, E., Redfern, S. A. T., Fyfe, C. A. and Strobl, H. (1987) Structural
542 States of Mg-Cordierite I: Order Parameters from Synchrotron X-Ray and
543 NMR Data. *Physics and Chemistry of Minerals*, 14, 446-454.
- 544 Rigby, M.J., Droop, G.T.R., and Bromiley, G.D. (2008) Variations in fluid activity
545 across the Etive thermal aureole, Scotland: evidence from cordierite volatile
546 contents. *Journal of Metamorphic Geology*, 26, 331-346.
- 547 Rodriguez-Carvajal, J. (2011) FullProf.2k, Version 5.20, Institut Laue-Langevin,
548 Grenoble, France.
- 549 Smith, D.C. (2005) The RAMANITA© method for non-destructive and in situ semi-
550 quantitative chemical analysis of mineral solid-solutions by multidimensional
551 calibration of Raman wave number shifts. *Spectrochimica Acta Part A*, 61,
552 2299-2314.
- 553 Stalder, R., Kronz, A., and Schmidt, B.C. (2009) Raman spectroscopy of synthetic
554 (Mg,Fe)SiO₃ single crystals. An analytical tool for natural orthopyroxenes.
555 *European Journal of Mineralogy*, 21, 27-32.
- 556 Vry, J.K., Brown, P.E., and Valley, J.W. (1990) Cordierite volatile content and the role
557 of CO₂ in high-grade metamorphism. *American Mineralogist*, 75, 71-88.
- 558 Wallace, J. H. and Wenk, H.R. (1980) Structure variation in low cordierites. *American*
559 *Mineralogist*, 65, 96-111.
- 560 Weikusat, C., Miletich, R., Glasmacher, U.A., Trautmann, C., and Neumann, R.
561 (2010) Heavy-ion irradiation on crystallographically oriented cordierite and the

562 conversion of molecular CO₂ to CO: a Raman spectroscopic study. *Physics*
563 *and Chemistry of Minerals*, 37, 417-424.

564 Werheit, H., Filipov, V., Shirai, K., Dekura, H., Shitsevalova, N., Schwarz, U., and
565 Armbruster, M. (2011) Raman scattering and isotopic phonon effects in
566 dodecaborides. *Journal of Physics: Condensed Matter*, 23(6), 065403-1-
567 06503-26.

568 Yakubovich, O.V., Massa, V., Pekov, I.V., Gavrilenko, P.G., and Chukanov, N.V.
569 (2004) Crystal Structure of the Na-, Ca-, Be-Cordierite and Crystallochemical
570 Regularities in the Cordierite-Sekaninaite Series. *Crystallography Reports*, 49,
571 953-963.

572

573

574

575

576

577

578

579

580

581

582

583

584

585

586

587

588 **Figure captions:**

589

590 **FIGURE 1.** Unpolarized Raman spectra of disordered, hexagonal (bottom) and
591 ordered, orthorhombic modifications (top) of Mg-Fe-cordierite with $X_{\text{Fe}} = 0, 0.49$ and 1
592 over the range of $100 - 1250 \text{ cm}^{-1}$. The positions of the peaks A – F in Mg-cordierite
593 are indicated by vertical stippled lines. The position of C' is indicated by a vertical
594 solid line.

595

596 **FIGURE 2 A – F.** Resulting calibration diagrams. The diagrams show the peak shift of
597 the peaks A – F towards lower wavenumbers as a function of $\text{Fe}/(\text{Fe} + \text{Mg})$ based on
598 the samples listed in Table 1. The error bars show the maximum 2σ standard
599 deviations (calculated for the Fe-end-member).

600

601 **FIGURE 3 A and B.** The figures show the splitting of the peaks in the area of 575 cm^{-1}
602 as a consequence of Al-Si ordering in Fe-cordierite (A) and the intensities of the type-
603 1 water peak at 3597 cm^{-1} (B) over a distance of $80 \mu\text{m}$ from the rim towards the
604 interior of the crystal.

605

606 **FIGURE 4.** Raman shift of band D. The open circles represent the data as a function of
607 X_{Fe} . The black line is the linear regression to the data. Six natural cordierite samples
608 from Bertoldi et al. (2004) with $X_{\text{Fe}} 0.04-0.76$ (black diamonds) are also shown in the
609 diagram. The error bars show the maximum 2σ standard deviations (calculated for
610 the Fe-end-member).

611

612 **Tables:**

613 **TABLE 1.** Electron microprobe analysis of 16 synthetic hydrous cordierite samples

Sample	1	2	3	4	5	6	7	8
Name	12.5h#7	33.4#5	33.4#2	33.4#6	33.7.2#2.2	33.7.2#5	33.7.2#2.1	29.2#1
SiO ₂	50.03(36)	48.61(33)	48.72(33)	48.43(33)	48.60(33)	47.73(32)	47.71(32)	48.92(34)
Al ₂ O ₃	33.82(28)	32.94(26)	33.64(26)	33.36(26)	32.13(26)	32.84(26)	33.03(26)	31.96(26)
FeO	n.d.	3.48(12)	6.00(16)	6.40(16)	7.44(17)	7.62(18)	8.21(18)	11.34(22)
MgO	13.85(21)	11.67(17)	9.08(15)	8.98(15)	9.03(15)	8.72(15)	8.08(14)	6.64(14)
Total	97.70(50)	96.70(47)	97.44(47)	97.17(47)	97.20(48)	96.91(47)	97.03(47)	98.86(50)
Si	4.988(36)	4.978(34)	4.998(34)	4.993(34)	5.037(34)	4.969(34)	4.972(34)	5.069(36)
Al	3.975(33)	3.976(32)	4.068(32)	4.054(32)	3.924(31)	4.030(32)	4.057(32)	3.903(32)
Fe	n.d.	0.298(11)	0.515(13)	0.552(14)	0.645(15)	0.663(15)	0.715(16)	0.982(19)
Mg	2.058(31)	1.781(26)	1.389(23)	1.38(23)	1.395(24)	1.353(23)	1.255(23)	1.025(22)
X _{Fe}	0.00	0.14	0.27	0.29	0.32	0.33	0.36	0.49

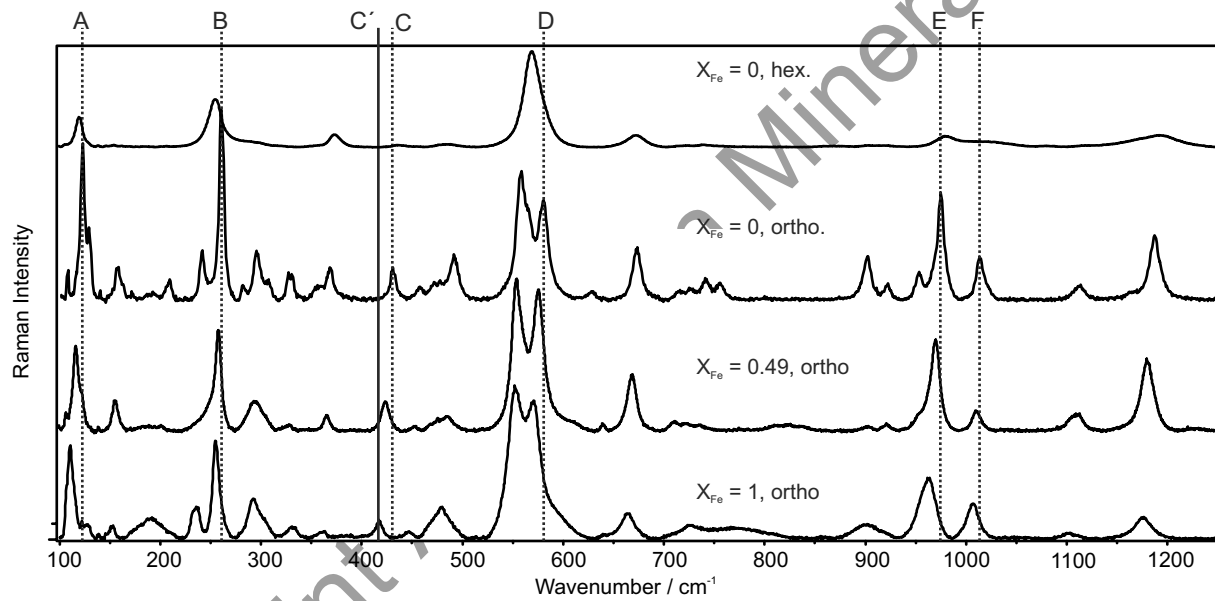
Sample	9	10	11	12	13	14	15	16
Name	30.1B1_2	29.2#3	29.2#2	31.2#6r	31.2#5r	37#1_3	38	26.5#8
SiO ₂	48.26(34)	47.9(34)	47.86(34)	45.16(32)	44.99(32)	47.45(25)	46.44(24)	45.96(32)
Al ₂ O ₃	32.36(27)	31.73(26)	31.66(26)	32.53(26)	32.26(26)	32.25(20)	30.84(20)	30.64(25)
FeO	11.25(21)	12.47(22)	13.18(23)	14.23(24)	14.46(24)	16.65(36)	17.68(37)	21.09(29)
MgO	6.57(14)	5.33(13)	4.82(12)	4.05(11)	3.97(11)	3.04(08)	2.42(07)	n.d.
Total	98.44(50)	97.43(50)	97.52(50)	95.97(49)	95.68(49)	99.39(49)	97.38(49)	97.69(50)
Si	5.023(35)	5.063(35)	5.070(36)	4.904(34)	4.907(34)	5.011(26)	5.034(26)	5.053(35)
Al	3.97(33)	3.954(32)	3.953(32)	4.163(33)	4.147(33)	4.037(25)	3.95(25)	3.97(33)
Fe	0.979(19)	1.102(20)	1.168(21)	1.292(21)	1.319(22)	1.491(32)	1.613(34)	1.94(26)
Mg	1.019(21)	0.841(20)	0.762(19)	0.656(18)	0.645(17)	0.498(12)	0.402(11)	n.d.
X _{Fe}	0.49	0.57	0.61	0.66	0.67	0.75	0.80	1.00

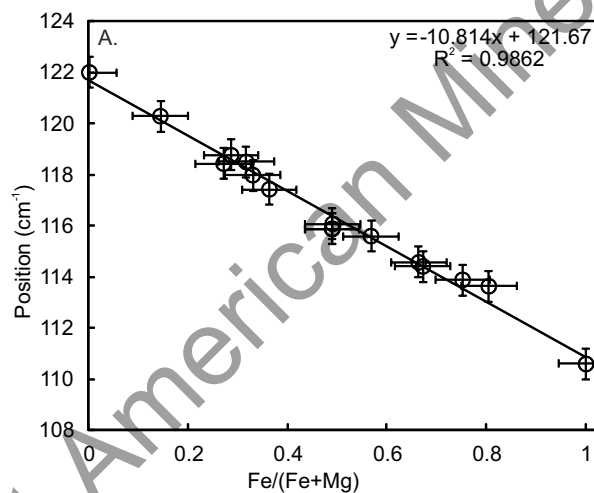
Note: the chemical formulae are normalized to 18 oxygens. X_{Fe} = Fe/(Fe + Mg); n.d.: not detected.

The numbers in brackets are 2σ standard deviations in terms of the last two digits.

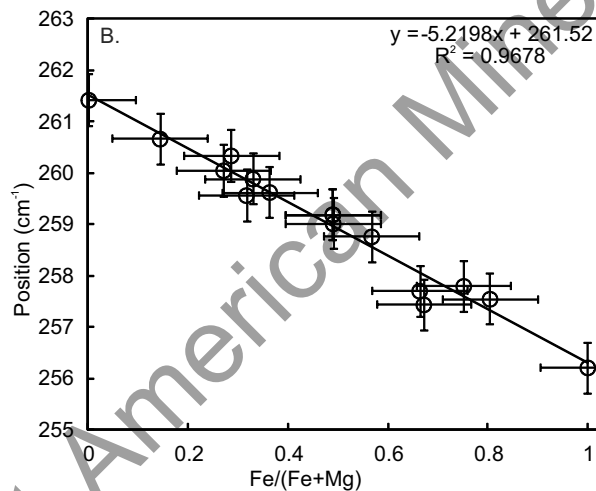
614

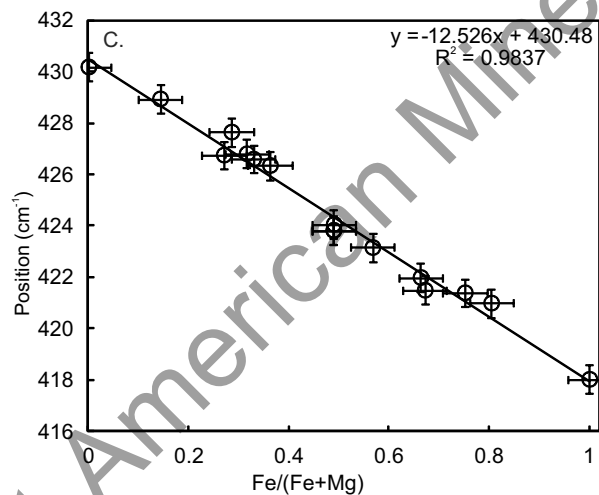
615

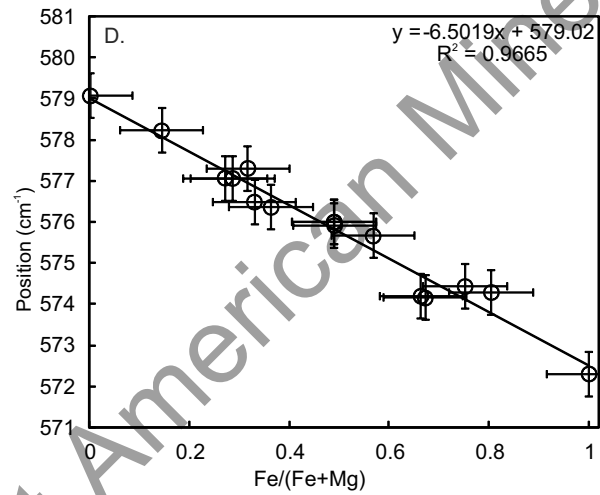


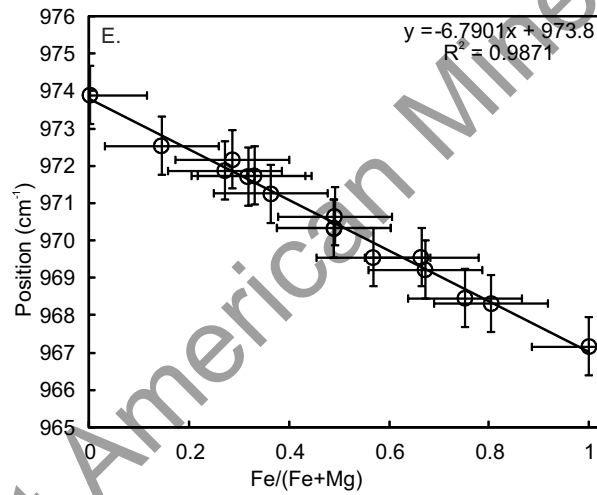


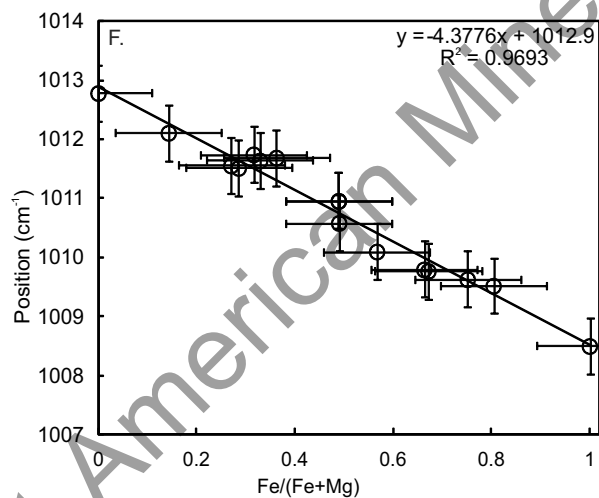
Preprint American Mineralogist

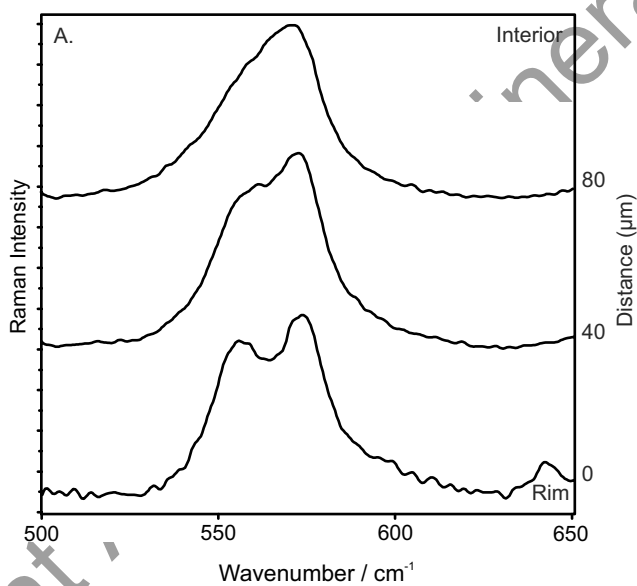


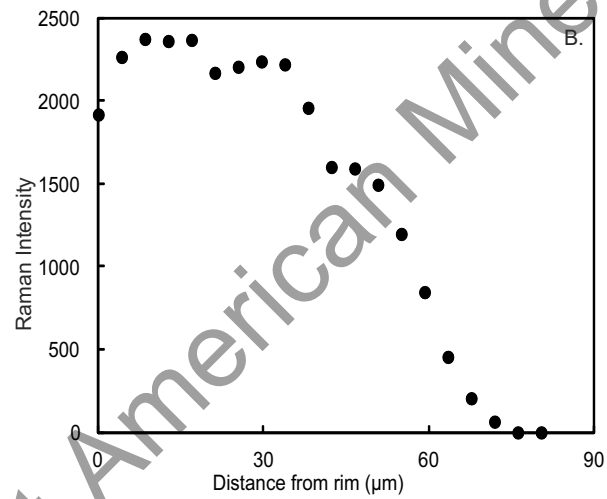


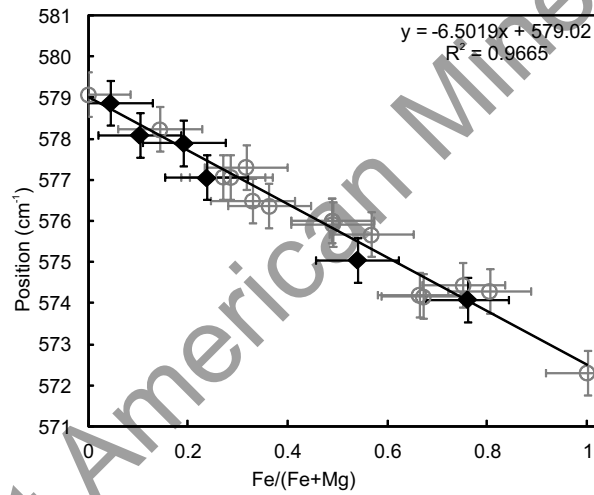












Preprint American Mineralogist